https://doi.org/10.2352/ISSN.2470-1173.2020.14.COIMG-250

Void detection and fiber extraction for statistical characterization of fiber-reinforced polymers

***Camilo Aguilar*[1], *Imad A. Hanhan*[2], *Ronald F. Agyei*[2], *Michael D. Sangid*[2], *Mary Comer*[1]**
[1] ***School of Electrical and Computer Engineering,*** [2] ***School of Aeronautics and Astronautics; Purdue University, West Lafayette, IN, USA***

Abstract

In this paper we propose a surrogate approach to extract fibers and voids from polymer matrix composites by combining results obtained from model-based methods to train convolutional neural networks. This approach focuses on microscopy images where labeled data is not readily available, but purely model based approaches can be too slow due to their computational complexity. In addition, we propose an encoder-decoder alternative to a fiber instance segmentation paradigm, showing a speed-up in training and inference times without a significant decrease in accuracy with respect to alternative methods. The neural networks approach represent a significant speedup over model based approaches and can correctly capture most fibers and voids in large volumes for further statistical analysis of the data.

Introduction

In recent years, materials researchers have proposed novel fiber-reinforced polymers as lightweight substitutes for certain metals. These materials are often comprised of glass or carbon fibers, polymer matrix, and voids formed due to entrapped gasses during the manufacturing process. Fig. 1 denotes two different fiber reinforced composites and their cross sections. Generally, brighter colors represent fibers, gray color represents the matrix, and voids are represented as irregular shapes with dark contours.

Experiments developing novel materials such as fiber-reinforced polymers often require detailed structural and mechanical characterization of the material properties. Structural characterization requires the extraction of information such as volume ratio, fiber length, fiber orientation, void volume, and intra-element interaction. These properties can directly affect the materials behavior and help to predict the material's response to external mechanical forces.

Many researchers have proposed solutions to extract structural information from volumetric representations of fiber-reinforced polymers. For example, multiple projects have used morphological filters and watershed to extract fibers [1], yet this problem presents issues detecting thin fibers. Similarly, [2] proposed a multi-view fiber fitting based on 2D pre-segmentation and 2D multi-slice ellipse fitting; however this method relies on characterizing fiber cross sections for different axes with 2D ellipses. Also, [3] proposed to use a connected tube marked point process model to extract fibers. This approach proved promising but non-scalable to large volumes due to the required time to find each tube. Finally, [4] proposed an embedded learning method to extract fibers from composite materials; however this approach requires pre-labeled data.

On the other hand, few methods have been proposed to extract voids from tomographic images. This occurs due to the irregular shape and arbitrary sizes that voids can exhibit in 3D. Some researchers proposed threshold segmentation, however this approach does not work well for large voids [5] [6]. The work in [7] proposed finding voids from phased arrays but in this paper we only deal with absorption images. In addition, [8] proposed an active contour framework embedded in a marked point process to extract voids but the computational complexity of such a method makes this approach infeasible for large volumetric data.

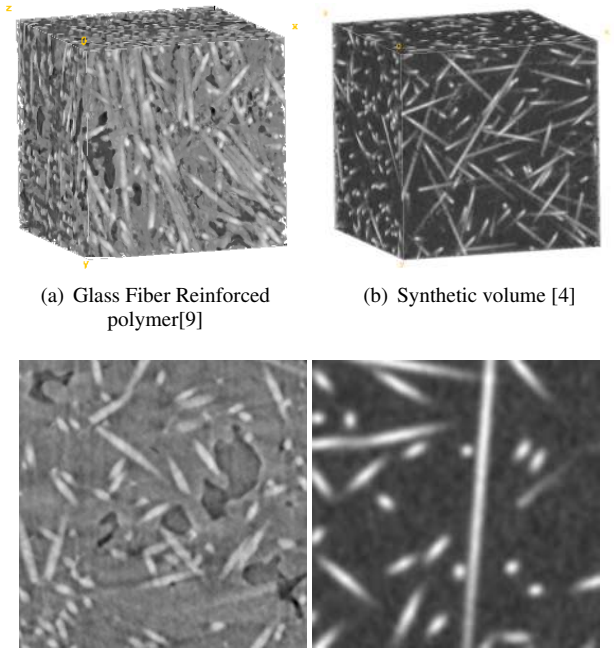

(a) Glass Fiber Reinforced polymer[9]

(b) Synthetic volume [4]

(c) Cross Section of (a)

(d) Cross Section of (b)

Figure 1. *Example of different fiber reinforced composite materials*

In this paper, we propose a surrogate approach which incorporates model-based methods on subvolumes and uses their results to train a neural network. This approach takes into account the lack of labeled data but also exploits the inference parallelization of using convolutional neural networks. In addition, we propose an encoder-decoder architecture to perform instance segmentation in order to speed up training and inference times.

Model Based Methods: Marked Point Process

The marked point process(MPP) is a probabilistic approach that models an image as a set of objects represented by the realization of a point process $\chi = \{k_1, k_2, \ldots, k_n\}$, where each point $k \subset \mathbb{R}^D$ is assigned a mark $m \in M$ to represent its geometry. The mark space M defines the object geometric parameters; for example, in the case of a disk, the mark space is defined as $M = [R_{min}, R_{max}]$, where R_{min} and R_{max} denote the minimum and maximum disk radius. A realization of a marked point process is defined as $\mathbf{w} = \{\omega_1, \omega_2, \ldots \omega_n\} \subset K \times M$, where $\omega_i = (k_i, m_i)$ denotes the i^{th} object at location k_i with mark m_i.

Fibers: Connected Tube Marked Point Process

We used the 3D extension of the connected tube MPP model proposed in [3] to detect fibers. This approach defines the mark space as $M = [R_{min}, R_{max}] \times [L_{min}, L_{max}] \times [\theta_{min}, \theta_{max} \times [\phi_{min}, \phi_{max}]$ and proposed a prior model to encourage long tubes, and connections between nearby short tubes. Fig. 2(a) and Fig. 2(b) shows a volume and 3D results of this approach applied to a glass fiber reinforced polymer. This approach can model fibers by detecting several tubes connected by their end points. We followed the procedure listed in [3] in order to set the model parameters.

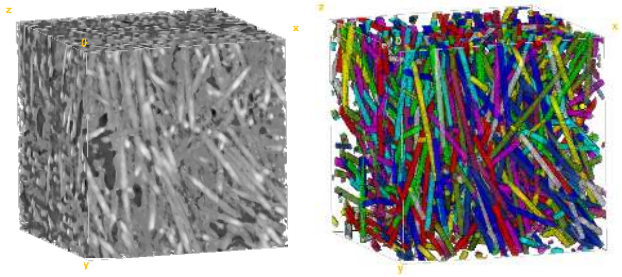

(a) Glass Fiber Reinforced polymer[9] (b) Connected Tube MPP [3]

Figure 2. *Sample Connected-Tube MPP Results*

Voids: Hybrid-Level sets and Active Contours

We detected voids using a variation of an MPP model that represents objects with disks of marks $M = [R_{min}, R_{max}]$, and deforms the disks with an active contour energy. Fig. 3(b) denotes a sample initial disk deformed with an active contour energy E_{ac} [8]. This approach was initially proposed by [10] and extended by [8]. We followed the hybrid level sets energy proposed by [11] and the level set deformation procedure in order to deform the contour. This hybrid contour model takes into account image intensity and object edges in order to converge to darker regions or regions with defined contours. Fig. 3(c) denotes a sample 2D cross section of a fiber reinforced polymer, and its detected voids.

One drawback of combining an MPP with level sets is that the computational requirements used to deform the contours increase exponentially with an increase of dimensions. Therefore, we detected voids in successive 2D slices, and used 3D smoothing filters to merge the results into a 3D structure. This approach is denoted in Fig. 3(d).

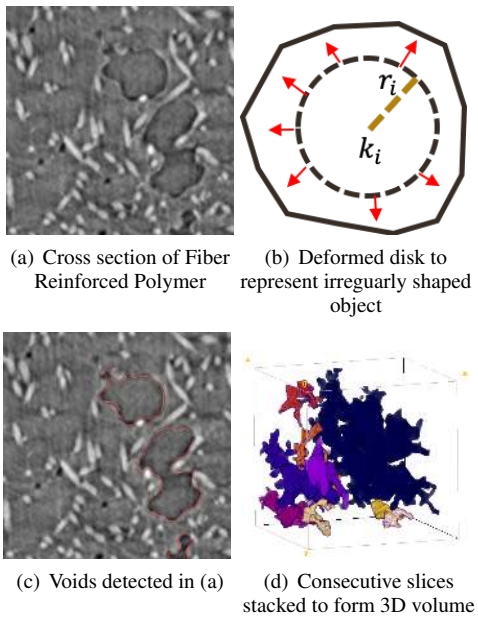

(a) Cross section of Fiber Reinforced Polymer (b) Deformed disk to represent irregularly shaped object

(c) Voids detected in (a) (d) Consecutive slices stacked to form 3D volume

Figure 3. *Results of Model-Based void detection*

Surrogate approach with Convolutional Neural Networks

Despite the promising results, MPP models rely on stochastic sampling for optimization. This approach can result in extensive computational burdens in order to find an optimal object configuration. This issue could make the inference of very large volumetric datasets unfeasible. In addition, the proposed model based methods detect fibers and voids independently and the results are superimposed; however, both results could yield discrepancies such as classifying a voxel as both fiber and void. In this section, we propose the use of neural networks to tackle both the object detection speed-up and the merging of fiber and void detection into a unified method. We propose to use the combined model-based results as labeled data to train neural networks to segment instances of objects in 3D. This approach is depicted in Fig. 4.

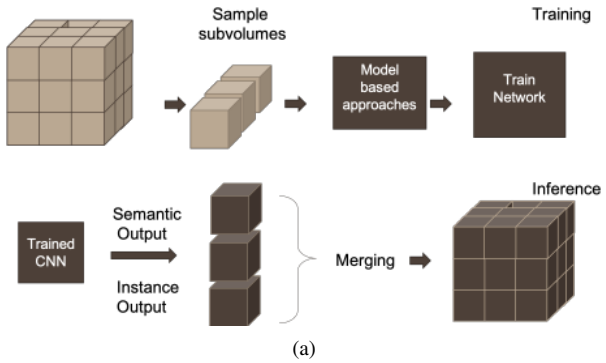

(a)

Figure 4. *Proposed surrogate approach*

Encoder-Decoder Embedding Instance Segmentation

Multiple projects have proposed instance segmentation approaches such as object proposal based [12] detection; however, multiple fibers have a curved structure that cannot be accurately represented with a bounding box. Similarly, a popular approach such as deep watershed [13] could fail to approximate a watershed energy for fibers with small radius. In this work, we explore further the work done in fiber embedding segmentation [4]. This method consists of tiling images into cubes of size $32 \times 32 \times 32$ voxels and using a fully convolutional network network with 2 output channels to classify pixels into foreground and background. Then, a similar network but with 12 output channels finds a mapping of foreground pixels into distant clusters in an embedded space. We propose an extension to this work by using an encoder-decoder architecture. This architecture represents both a speed-up in inference times over the fully convolutional network and a reducion in memory requirements. This approach allowed us to increase the window size from $32 \times 32 \times 32$ voxels to $128 \times 128 \times 128$ voxels without compromising performance. Fig.5 represents the network architecture. We followed the architecture proposed by [14] for semantic segmentation, and the same architecture but with 12 output channels for instance segmentation.

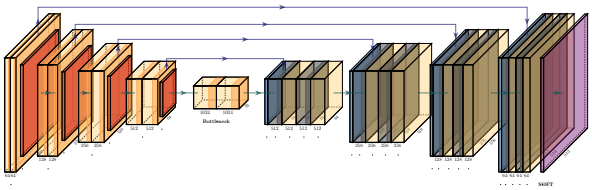

(a)

Figure 5. *Encoder Decoder Network Architecture proposed by [14]*

Network Training

Semantic Segmentation

We used the weighted cross entropy loss function in order to train the semantic segmentation network. The cross entropy function is defined as:

$$Loss_{Semantic} = -\sum_{i=0}^{L-1} w_i t_i log(s_i) \tag{1}$$

where L is the number of classes, t_i is the ground truth label, s_i is the output score for class i, and w_i is a predefined weight. We trained the network with $L = 3$ for the dataset depicted in Fig. 1(a), with $w_0 = 1$ (matrix),$w_1 = 10$(fiber) ,$w_2 = 20$ (void) and $L = 2$ for the dataset depicted in Fig. 1(b) with $w_0 = 1$, and $w_1 = 5$. These weights were chosen from the voxel ratios between classes available in the labeled data. We used the Adam optimizer with a leaning rate $lr = 0.0001$ and we trained the network for 1000 epochs, feeding 30 cropped subvolumes in each epoch.

Instance Segmentation

For instance segmentation, we followed the approach taken by [4]; therefore we used a similar network to our semantic segmentation network, but with 12 output channels. The instance segmentation loss function is defined as follows:

$$Loss_{instance} = \alpha L_{pull} + \beta L_{push} + \gamma L_{regularization} \tag{2}$$

The first part of the loss function teaches the network to pull the embedding outputs of an instance towards the center of a cluster and is defined as $L_{pull} = \frac{1}{C}\sum_{c=1}^{C}\sum_{x_i=1,x_i\in c}^{N_c}(||x_i - \mu_c|| - \delta_v)_+^2$, where $(x)_+ = max(0,x)$, C is the number of instances, x_i is the output of the embedding network for the i^{th} voxel that belongs to instance c, and $\mu_c = \frac{1}{N_c}\sum_{i=1}^{N_c} x_i$ is the mean embedding value for one specific instance with N_c voxels. In all our experiments, we set the hyper-parameter $\delta_v = 0.2$. This value could be translated to the euclidean distance parameter in clustering algorithms as the maximum distance to consider two points to belong to the same cluster.

The second term is in Eq. (2) has the purpose of teaching the network to push the centers of the clusters away from each other. This loss function is defined as $L_{push} = \frac{1}{(C)(C-1)}\sum_{i=1}^{C}\sum_{j=1,j\neq i}^{C}(\delta_d - ||\mu_i - \mu_j||)_+^2$. In all our experiments, we set $\delta_d = 5$. This parameter was chosen following the convention $\delta_d \gg \delta_v$.

The third part of the loss function is intended to regularize the mean embeddings and is defined as $L_{regularization} = \frac{1}{C}\sum_{i=1}^{C}||\mu_i||$.

This loss function only takes into account the foreground pixels previously classified by the semantic segmentation network. We used the Adam optimizer with learning rate $lr = 0.001$ and we trained the network during 2000 epochs with subvolumes cropped from the labeled data. We followed the parameter setting used by [4] and set the parameters $\alpha = 2$, $\beta = 2$, and $\gamma = 0.001$. Fig. 6 shows the learning procedure of the mapping network for different training iterations. Each color represents a distinct instance of a fiber. Finally a clustering algorithm (DBSCAN [15]) assigns each pixel to clusters that represent fiber instances.

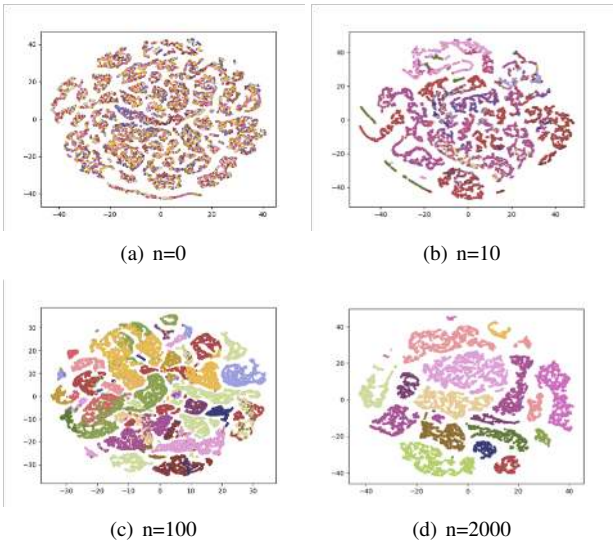

(a) n=0 (b) n=10

(c) n=100 (d) n=2000

Figure 6. *Embedded learning at different iterations. Images have been reduced to 2 dimensions using t-SNE [16] for visualization purposes*

Results

In this section we present results for the two datasets. The first dataset is experimental data and lacks ground truth, therefore our results are evaluated visually from sample cross sections. We used a second set of available labeled data for numeric evaluation and we considered three parameters: 1) voxel-wise segmentation accuracy, 2) fiber detection correctness, and 3) inference time.

We evaluate our method compared to the superimposed model-based results (Connected Tube MPP and Active Contours MPP), the fully convolutional network-based approach [4], our proposed encoder-decoder approach using the MPP results as training data and our proposed encoder-decoder approach using the true labels as labeled data (when available).

Experimental Data: Glass Fiber Reinforced Polymer

The first dataset was an X-ray micro-computed tomography scan of a glass fiber reinforced polypropylene [9] and represents glass fibers in a polypropylene matrix composite. The sample was imaged at $1.3\mu m$ of resolution and its dimensions are $2400 \times 2400 \times 1300$ voxels. In this paper, we used a subvolume of $301 \times 301 \times 301$ voxels for display purposes. It is worth noting we we used the connected tube MPP and active contours MPP to obtain labeled training data.

Semantic Segmentation

For semantic segmentation, we converted the superimposed MPP results to three classes denoted in Fig.7(b). These methods provided a starting point for the semantic segmentation, but they still presented noise in the results. For instance, Fig.7(b) shows a false void(blue) at the bottom left part of the image. Similarly, Fig.7(b) shows multiple missed fibers(green) near the center and left part of the image. This issue happens due to noise generated during the imaging and sample reconstruction procedure, and due to parameter calibration for both MPP approaches.

We trained both networks using the same training parameters, however we used a window size of $128 \times 128 \times 128$ voxels for our network, and we used a window size of $32 \times 32 \times 32$ voxels for the fully convolutional network. Both neural network approaches were able to segment all the voids and reduced the amounts of phantom voids that were detected in the model-based approaches. Additionally, the networks learned to segment fibers that were not segmented originally in the model-based methods; however, Fig. 7(c) shows the fully convolutional network presented over-segmentation of fibers. This issue leads to difficulty performing instance segmentation.

Fig. 7 denotes the results obtained from finding the semantic segmentation for 3 different approaches: Connected Tube MPP [3], Fully Convolutional Network[4], and our method. Fig 7(c) represents the output of our implementation of the work proposed by Konopczynski [4] trained with the MPP as labeled data.

Labeled Data: Low Resolution Fibrous Material

We tested our methods on a synthetic dataset [4] for numerical comparison. This dataset provides several real and synthetic fibrous volumes imaged at $3\mu m$ of resolution. We used the datasets R_HR3_1 and R_HR3_2 for training the networks, and we evaluated the results on multiple subvolumes of the dataset

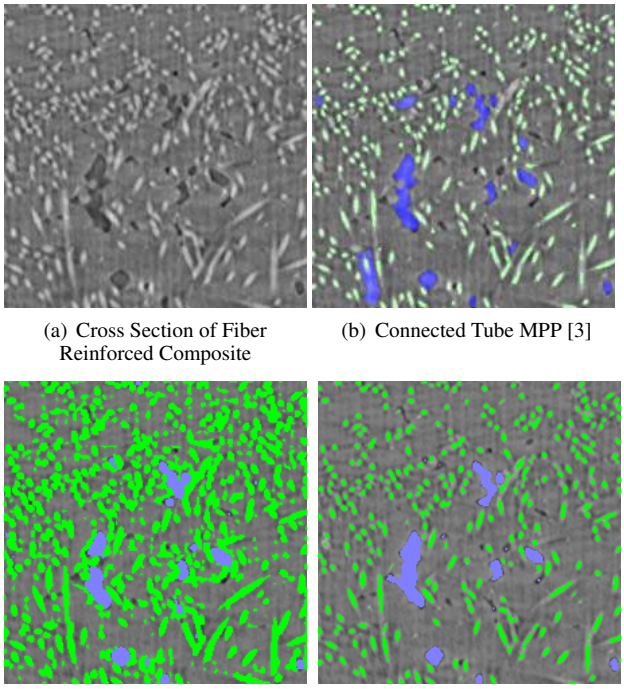

(a) Cross Section of Fiber Reinforced Composite

(b) Connected Tube MPP [3]

(c) Fully Convolutional Network [4]

(d) **Proposed Encoder-Decoder**

Figure 7. *Semantic Segmentation for polypropylene matrix composite. Fibers are represented green, voids are represented blue*

S_HR_5.35. We use only fiber data for validation since this dataset does not contain voids and we used subvolumes of size $600 \times 600 \times 600$ pixels for numerical and timing analysis.

Semantic Segmentation

For evaluation of semantic segmentation, we evaluated precision, recall and the f1 score, which is defined as:

$$f1 = \frac{2 * precision * recall}{precision + recall} \tag{3}$$

where $precision = \frac{TP}{TP+FP}$, and $recall = \frac{TP}{TP+FN}$, and TP denote true positives, FP denote false positives, and FN denote false negatives.

The results for the segmentation numerical comparison are depicted in Table 1. All the neural networks-based approaches present high recall values but low precision values. This occurs due to the over segmentation occurring at the fiber boundaries. On the other hand, the connected tube MPP has a larger precision but lower recall values. This issue could happen because the MPP models objects with basic geometries(tubes) and does not account for the fibers' surface roughness.

Quantitative Results

	Precision	Recall	f1
Connected Tube MPP	0.801	0.692	0.743
Embedded Learning [4]	0.547	0.986	0.704
Proposed-MPP	0.561	0.976	0.712
Proposed-label	0.662	0.972	0.787

Despite the different approaches proposed for segmentation, the maximum f1 score is 0.787 by the encoder-decoder network. The low scores happen mainly due to the ambiguity at fiber boundaries. However, it should be noted that, due to limitations in spatial resolution of physical imaging systems, it is often impossible for even materials experts to determine exact boundaries between different regions in a microstructure. We consider any pixel to be within $\sqrt{2}$ voxels from a fiber voxel to be a TP; similarly, we consider any segmented voxel farther than $\sqrt{2}$ voxels from a labeled fiber voxel to be a FP, and we consider any missed fiber voxel farther than $\sqrt{2}$ from a labeled fiber voxel to be a FN. The results with the this "relaxed-boundary" scoring are presented in Table 2.

Relaxed-Boundary Quantitative Results

	Precision	Recall	f1
Connected Tube MPP	0.979	0.966	0.972
Fully Convolutional Network [4]	0.918	0.999	0.957
Proposed-MPP	0.990	0.911	0.949
Proposed-label	0.894	0.999	0.944

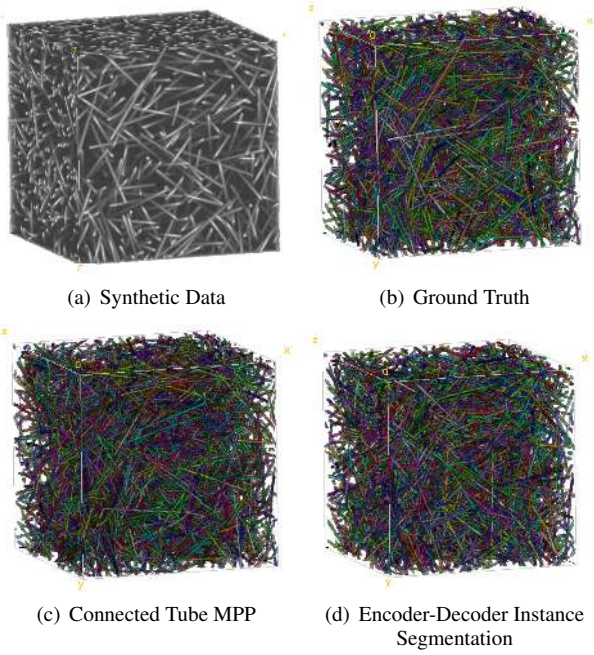

(a) Synthetic Data (b) Ground Truth

(c) Connected Tube MPP (d) Encoder-Decoder Instance Segmentation

Figure 8. *Instance Segmentation*

Instance Segmentation

For instance segmentation, we considered 3 common cases in fiber detection: the fiber is detected correctly, the fiber is artificially broken, or the fiber is missed. We say a fiber is detected correctly if the IoU between the detected object and the ground truth label is greater than 0.5. We consider a fiber to be broken if multiple detected fibers fit into the ground truth fiber, such that the total IoU is greater than 0.5. We say a fiber is missed if either the total IoU of overlapping detected objects and ground truth label is less than 0.5, or if the fiber was merged with a nearby fiber. Fig. 8 shows the results for a subvolume of $600 \times 600 \times 600$ voxels using both MPP and Connected Tube MPP. Table 3 denotes the fiber detection numerical results using different approaches. In terms of detecting fibers at least partially (including the detected and broken cases), the approach with best results was the Connected Tube MPP which missed only 0.6% of fibers. The next best result uses the proposed encoder-decoder network using the labeled data for training, which missed 12% of fibers. Finally, the Fully Convolutional Network approach together with the proposed method trained with MPP labels showed worse performance a 74% and 78% of fibers correctly detected.

Required Time

We performed timing comparisons for volume inference for volumes of size $100^3, 200^3, 400^3$, and 600^3. Fig. 9 denotes the different timing measurements for each method at different subvolumes. The connected-tube MPP model was implemented in C++ programming language and was timed using a single core on an Intel(R) Core(TM) i9-9900X CPU processor running at 3.50GHz. Both neural networks were implemented in pytorch and tested in the same machine with an NVIDIA TITAN RTX GPU. The encoder/decoder architecture represented a 10 times speedup over the connected tube MPP, and a 4 times speedup over the fully convolutional network architecture.

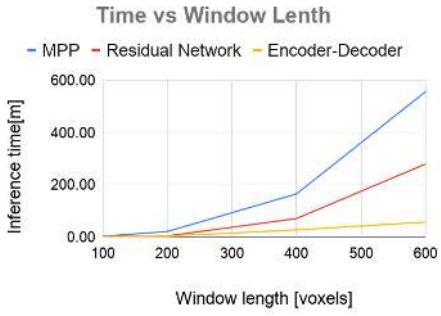

Figure 9. *Time Difference*

Conclusion

We presented an approach to train a neural network with model based approaches in order to detect objects in microscopy images. We also validated numerically the approach using data openly available. Our approach was able to detect both fibers and voids, and it presented semantic and instance segmentation results that could compete with model-based approaches, despite being significantly faster.

Acknowledgments

The authors would like to acknowledge the support of the National Science Foundation through grant NSF CMMI MoM 16-62554. Also, the authors would like to thank Dr. Xianghui Xiao for assistance with the tomography characterization at the Advanced Photon Source. The use of the Advance Photon Source is granted by the US Department of Energy, Office of Science, and Office of Basic Energy Sciences under Contract No. DE-AC02 06CH11357.

Fiber Detection Results

	Number of Fibers	Detected	Broken	Missed
MPP	748	653	90	5
Fully Convolutional Network [4]	748	559	17	172
Proposed-MPP	748	588	0	160
Proposed-label	748	651	10	96

References

[1] X. Huang, D. Wen, Y. Zhao, Q. Wang, W. Zhou, and D. Deng, "Skeleton-based tracing of curved fibers from 3d x-ray microtomographic imaging," *Results in Physics*, vol. 6, pp. 170 – 177, 2016.

[2] R. F. Agyei, B. Sharma, and M. Sangid, "Investigating Sub-surface Microstructure in Fiber Reinforced Polymer Composites via X-Ray Tomography Characterization," *57th AIAA/ASCE/AHS/ASC Structures, Structural Dynamics, and Materials Conference*, no. January, pp. 1–6, 2016. [Online]. Available: http://arc.aiaa.org/doi/10.2514/6.2016-0409

[3] T. Li, M. Comer, and J. Zerubia, "A Connected-Tube MPP Model for Object Detection with Application to Materials and Remotely-Sensed Images," *Proceedings - International Conference on Image Processing, ICIP*, pp. 1323–1327, 2018.

[4] T. K. Konopczynski, T. Kröger, L. Zheng, and J. Hesser, "Instance segmentation of fibers from low resolution ct scans via 3d deep embedding learning," in *BMVC*, 2018.

[5] A. Madra, N. E. Hajj, and M. Benzeggagh, "X-ray microtomography applications for quantitative and qualitative analysis of porosity in woven glass fiber reinforced thermoplastic," *Composites Science and Technology*, vol. 95, pp. 50 – 58, 2014.

[6] I. Hanhan and M. D. Sangid, "ModLayer: A MATLAB GUI Drawing Segmentation Tool for Visualizing and Classifying 3D Data," *Integrating Materials and Manufacturing Innovation*, vol. 8, no. 4, pp. 468–475, 2019. [Online]. Available: https://doi.org/10.1007/s40192-019-00160-5

[7] C. Nageswaran, C. R. Bird, and R. Takahashi, "Phased array scanning of artificial and impact damage in carbon fibre reinforced plastic (cfrp)," 2006.

[8] C. Aguilar and M. Comer, "A Marked Point Process Model Incorporating Active Contours Boundary Energy," *Electronic Imaging*, vol. 2018, no. 15, pp. 230–1–2304, 2018.

[9] R. F. Agyei and M. D. Sangid, "A supervised iterative approach to 3D microstructure reconstruction from acquired tomographic data of heterogeneous fibrous systems," *Composite Structures*, vol. 206, no. January, pp. 234–246, 2018. [Online]. Available: https://doi.org/10.1016/j.compstruct.2018.08.029

[10] M. Kulikova, I. Jermyn, X. Descombes, E. Zhizhina, and J. Zerubia, "Extraction of arbitrarily-shaped objects using stochastic multiple birth-and-death dynamics and active contours," *Electronic Imaging*, vol. 7533, 2010. [Online]. Available: https://doi.org/10.1117/12.839191

[11] Z. Yan, B. J. Matuszewski, L. K. Shark, and C. J. Moore, "Medical image segmentation using new hybrid level-set method," *Proceedings - 5th International Conference BioMedical Visualization, Information Visualization in Medical and Biomedical Informatics, MediVis 2008*, no. 1, pp. 71–76, 2008.

[12] S. Ren, K. He, R. Girshick, and J. Sun, "Faster r-cnn: Towards real-time object detection with region proposal networks," in *Advances in Neural Information Processing Systems 28*, C. Cortes, N. D. Lawrence, D. D. Lee, M. Sugiyama, and R. Garnett, Eds. Curran Associates, Inc., 2015, pp. 91–99. [Online]. Available: http://papers.nips.cc/paper/5638-faster-r-cnn-towards-real-time-object-detection-with-region-proposal-networks.pdf

[13] M. Bai and R. Urtasun, "Deep watershed transform for instance segmentation," in *2017 IEEE Conference on Computer Vision and Pattern Recognition (CVPR)*, July 2017, pp. 2858–2866.

[14] O. Ronneberger, P. Fischer, and T. Brox, "U-net: Convolutional networks for biomedical image segmentation," *Lecture Notes in Computer Science (including subseries Lecture Notes in Artificial Intelligence and Lecture Notes in Bioinformatics)*, vol. 9351, pp. 234–241, 2015.

[15] M. Hahsler, M. Piekenbrock, and D. Doran, "dbscan: Fast density-based clustering with R," *Journal of Statistical Software*, vol. 91, no. 1, pp. 1–30, 2019.

[16] L. van der Maaten and G. Hinton, "Visualizing high-dimensional data using t-sne," *Journal of Machine Learning Research*, vol. 9, pp. 2579–2605, 2008.

JOIN US AT THE NEXT EI!

IS&T International Symposium on

Electronic Imaging

SCIENCE AND TECHNOLOGY

Imaging across applications . . . Where industry and academia meet!

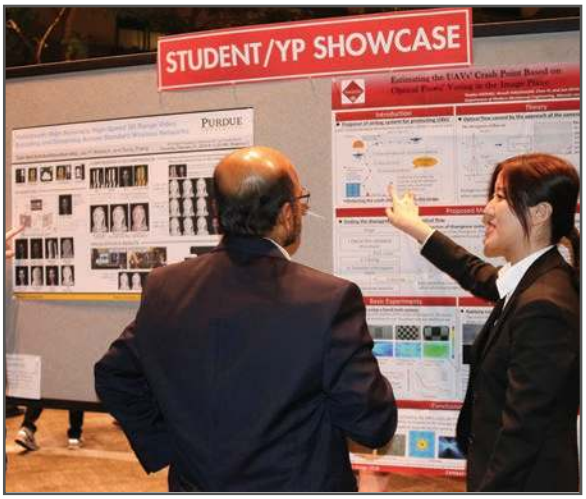

• SHORT COURSES • EXHIBITS • DEMONSTRATION SESSION • PLENARY TALKS •
• INTERACTIVE PAPER SESSION • SPECIAL EVENTS • TECHNICAL SESSIONS •

www.electronicimaging.org

IS&T
imaging.org